



## RESEARCH ARTICLE

# Site-selective substitution and resulting magnetism in arc-melted perovskite $ATiO_{3-\delta}$ ( $A = Ca, Sr, Ba$ )

Songhak Yoon<sup>1</sup> | Wenjie Xie<sup>2</sup>  | Xingxing Xiao<sup>2</sup> | Stefano Checchia<sup>3</sup> |  
 Mauro Coduri<sup>3,4</sup> | Peter Schuetzenduebe<sup>5</sup> | Marc Widenmeyer<sup>2</sup> |  
 Stefan G. Ebbinghaus<sup>6</sup> | Benjamin Balke<sup>1</sup> | Anke Weidenkaff<sup>1,2</sup> | Gisela Schütz<sup>5</sup> |  
 Kwanghyo Son<sup>5,7</sup> 

<sup>1</sup>Fraunhofer Research Institution for Materials Recycling and Resource Strategies IWKS, Hanau, Germany

<sup>2</sup>Department of Materials and Earth Sciences Materials, and Resources, Technical University of Darmstadt, Darmstadt, Germany

<sup>3</sup>European Synchrotron Radiation Facility, Grenoble, France

<sup>4</sup>Department of Chemistry, University of Pavia, Pavia, Italy

<sup>5</sup>Department of Modern Magnetic Systems, Max Planck Institute for Intelligent Systems, Stuttgart, Germany

<sup>6</sup>Institute of Chemistry, Martin Luther University, Halle-Wittenberg, Halle, Germany

<sup>7</sup>Department of Physics Education, Kongju National University, Gongju, South Korea

## Correspondence

Songhak Yoon, Fraunhofer Research Institution for Materials Recycling and Resource Strategies IWKS, Aschaffener Straße 121, 63457 Hanau, Germany.

Email:

[song.hak.yoon@iwks.fraunhofer.de](mailto:song.hak.yoon@iwks.fraunhofer.de)

Kwanghyo Son, Department of Modern Magnetic Systems, Max Planck Institute for Intelligent Systems, Heisenbergstraße 3, 70569 Stuttgart, Germany.

Email: [kson@kongju.ac.kr](mailto:kson@kongju.ac.kr)

## Abstract

Magnetic properties in perovskite titanates  $ATiO_{3-\delta}$  ( $A = Ca, Sr, Ba$ ) were investigated before and after arc melting. Crystal structure analysis was conducted by powder synchrotron X-ray diffraction with Rietveld refinements. Quantitative chemical element analysis was carried out by X-ray photoelectron spectroscopy. Magnetic measurements were conducted by vibrating sample magnetometer and X-ray magnetic circular dichroism (XMCD). The magnetic properties are found to be affected by impurities of 3d elements such as Fe, Co, and Ni. Depending on the composition and crystal structure, the occupation of the magnetic ions in perovskite titanates is selectively varied, which is interpreted to be the origin of the different magnetic behaviors in arc-melted perovskite titanates  $ATiO_{3-\delta}$  ( $A = Ca, Sr, Ba$ ). In addition, both formation of oxygen vacancies and the reduction of  $Ti^{4+}$  to  $Ti^{3+}$  during arc-melting also play a role as proven by XMCD. Nevertheless, preferential site occupation of magnetic impurities is dominant in the magnetic properties of arc-melted perovskite  $ATiO_{3-\delta}$  ( $A = Ca, Sr, Ba$ ).

## KEYWORDS

arc-melting, magnetism, perovskite oxide, synchrotron X-ray diffraction, X-ray magnetic circular dichroism

This is an open access article under the terms of the [Creative Commons Attribution](https://creativecommons.org/licenses/by/4.0/) License, which permits use, distribution and reproduction in any medium, provided the original work is properly cited.

© 2023 The Authors. *Journal of the American Ceramic Society* published by Wiley Periodicals LLC on behalf of American Ceramic Society.

## 1 | INTRODUCTION

Perovskite-type oxides ( $ABO_3$ ) are one of the most intensely studied materials as they exhibit many fascinating and intriguing physical and chemical properties.<sup>1</sup> Due to the compositional flexibilities of perovskites with extensive substitution levels, physical and chemical properties can be effectively and precisely tuned.<sup>2–5</sup> In addition, through the design and control of very small changes in oxygen vacancy concentrations, optical, catalytic, electronic, ionic, and magnetic properties can be strongly affected and controlled.<sup>6–9</sup> Several strategies for the generation of oxygen vacancies in perovskites have been reported.<sup>10</sup>

Compared to conventional sintering, arc-melting is found to consume less power and energy compared to conventional heating methods which is beneficial for a circular economy.<sup>11</sup> The arc-melting method has been typically used for melting metals to form alloys<sup>12</sup> and is now fully recognized as one of the techniques to generate oxygen vacancies. The high-temperature electric arc heats the oxides to their melting point for only a few seconds, followed by rapid cooling to room temperature. These rapid melting and cooling processes effectively induce a high concentration of defects in the oxide. Ou et al. used the arc-melting technique to obtain defective metal oxides in order to narrow the bandgap of oxide semiconductors.<sup>13</sup> The arc-melting treatment can turn white  $TiO_2$  into black.<sup>14,15</sup> The solid solution  $La_{1-x}Sr_xTiO_3$  ( $0 \leq x \leq 1$ ) has been prepared by arc-melting of stoichiometric amounts of  $SrTiO_3$  and  $LaTiO_3$ .<sup>16</sup> A series of  $Nd_{1-x}A_xTiO_3$  ( $A = Ca, Sr, Ba; 0 \leq x \leq 1$ ) compounds has been synthesized and reported.<sup>17</sup> Connolly and Tilley have tried to synthesize the layered-perovskite  $Nd_nTi_nO_{3n+2}$  ( $n = 4.5 - 6.5$ ).<sup>18</sup> Gu et al. presented enhanced photocatalytic performances of  $SrTiO_3$  using laser-melting treatment.<sup>19</sup> Yu et al. extended this method for the preparation of defective  $SrTiO_3$  and confirmed that a large amount of oxygen vacancies have been implanted in the arc-melted  $SrTiO_3$ .<sup>20</sup>

Magnetization can be also induced by non-magnetic cations in oxides.<sup>21,22</sup> Zhang et al. investigated vacancy-induced magnetism in perovskite  $SrTiO_3$  by ab initio calculations.<sup>23</sup> By using an ion irradiation or laser annealing process, room-temperature ferromagnetism is observed in high-quality  $SrTiO_3$  single crystals.<sup>24,25</sup> Upon arc-melting, the color of  $SrTiO_3$  powder turned from white to dark gray, and the magnetic moment is about 10-fold increased, which was attributed to the introduced defects during arc-melting.<sup>20</sup> Even though many researchers have evidenced the magnetic properties of arc-melted  $SrTiO_3$ , neither systematic study nor detailed investigation of the origin of magnetic properties is reported on titanates  $ATiO_{3-\delta}$  ( $A = Ca, Sr, Ba$ ). We emphasize that the

modification of magnetic properties in a perovskite  $ABO_3$  compound arises not only from oxygen vacancies but also from selective substitutions on either the  $A$ -site or  $B$ -site.

In this study, we have applied the arc-melting technique for the synthesis of defective perovskite titanates  $ATiO_{3-\delta}$  ( $A = Ca, Sr, Ba$ ). In addition, a systematic study of the magnetic properties with the relationship between magnetic impurities and oxygen vacancies associated with  $Ti^{3+}$  in arc-melted perovskite titanates was conducted. With this study, we have shown that site-selective occupation of the magnetic  $3d$  impurities such as Fe, Co, and Ni play a dominant role in the magnetism of perovskite titanates  $ATiO_{3-\delta}$ .

## 2 | EXPERIMENTAL PROCEDURES

All powders,  $CaTiO_3$  (Alfa Aesar,  $\geq 99\%$ ),  $SrTiO_3$  (Sigma-Aldrich,  $\geq 99\%$ ), and  $BaTiO_3$  (Alfa Aesar,  $\geq 99\%$ ) were used directly without any further purification. Powders were pressed into pellets using a uniaxial press and placed on a water-cooled Cu substrate. The powders were heated under an Ar atmosphere to be melted by a high-energy arc. Followed by fast heating and melting, the samples were quenched to room temperature. The white pellets are congruently melted and transformed into bulk samples as exemplarily shown in Supporting Information S1. The inside of the arc-melted sample is entirely black and shiny. The arc-melted pellets were ground for further characterization.  $CaTiO_3$ ,  $SrTiO_3$ , and  $BaTiO_3$  samples before arc-melting are denoted as CTO, STO, and BTO, respectively, while the corresponding samples after arc-melting are denoted in the following as CTO\_arc, STO\_arc, and BTO\_arc, respectively.

Synchrotron high-resolution powder X-ray diffraction (XRD) patterns were obtained at the beamline ID22 of the European Synchrotron Radiation Facility (ESRF) with a wavelength of 0.35439 Å. The sample powders were sealed in quartz capillaries of 1.0 mm in diameter, and the diffraction patterns were recorded in the transmission modes at room temperature in a  $2\theta$  range of  $1-48^\circ$  with an angular step interval of  $0.002^\circ$ , using the setup equipped with crystal analyzers.<sup>26</sup> XRD patterns were analyzed in a  $2\theta$  range of  $3-32^\circ$  by the Rietveld refinement program *Fullprof.2k*. The Thompson-Cox-Hastings pseudo-Voigt function was chosen as profile function. Phase identification was performed by using the program *Malvern Panalytical HighScore*.

X-ray photoelectron spectroscopy (XPS) measurements were carried out in a Thermo VG Thetaprobe system (Thermo Fisher Scientific) employing monochromatic Al  $K\alpha$  X-ray radiation (1486.7 eV) applying an electrical power of 100 W. The X-ray spot size on the sample was about

400  $\mu\text{m}$  in diameter. An electron flood gun was employed for surface charge compensation. The samples were loaded into the ultra-high vacuum chamber one day before measurements. Survey spectra were recorded with a pass energy of 200 eV, and more detailed spectra of single elemental peaks were measured in snap scan mode afterward. The measured data were fitted using the routines included in the software *Avantage*.

DC magnetic properties were determined by means of a vibrating sample magnetometer (VSM, Quantum Design MPMS 3). Temperature dependence of the susceptibility was measured with field-cooled (FC) and zero-FC (ZFC) protocols in the temperature range of 3–300 K under a magnetic field of  $\mu_0 H = 0.1$  T. Further high temperature magnetic susceptibility data from 300 to 950 K were collected using a furnace the same applied field. Finally, field dependent measurements were conducted in the range of 7 T to  $-7$  T at various temperatures.

Both X-ray absorption spectroscopy (XAS) and X-ray magnetic circular dichroism (XMCD) at the  $\text{Ti-L}_{2,3}$  edge were performed at the synchrotron ANKA in KIT, Karlsruhe. All XAS and XMCD spectra were recorded in the total electron yield mode at WERA beamline with an energy resolution  $\Delta E/E = 2 \times 10^{-4}$ . The XMCD spectra were measured in an applied magnetic field of up to 2 T.

### 3 | RESULTS

Figure 1 shows the XRD patterns of both the pristine white powders and arc-melted black ones. All main reflections are found to be well-fitted by the respective perovskite oxides. As shown in Supporting Information S2, the comparison of the main reflection of each perovskite oxide before and after arc-melting clearly revealed that the full width at half maximum (FWHM) is reduced by ca. a factor of 2 after arc-melting, indicating the increase of crystallite sizes and/or decreased micro-strains in the lattice. No recognizable preferred orientations are observed and a more detailed analysis of FWHM is given in Supporting Information S2. More importantly, owing to the high flux and brilliance of the photon beam provided by synchrotron radiation at beamline ID22 of the ESRF, we could even detect secondary phases (Figure 1), which were hardly detectable by a laboratory X-ray diffractometer. Notably, the secondary phases are only visible in the pristine white powders, especially for CTO and BTO. The reflections which do not belong to the perovskite phase vanished after arc-melting. Details of phase identification are shown in Supporting Information S3. Anatase  $\text{TiO}_2$  was found for CTO, BTO, and STO as a main secondary phase. Additional secondary phases in the samples before arc-melting

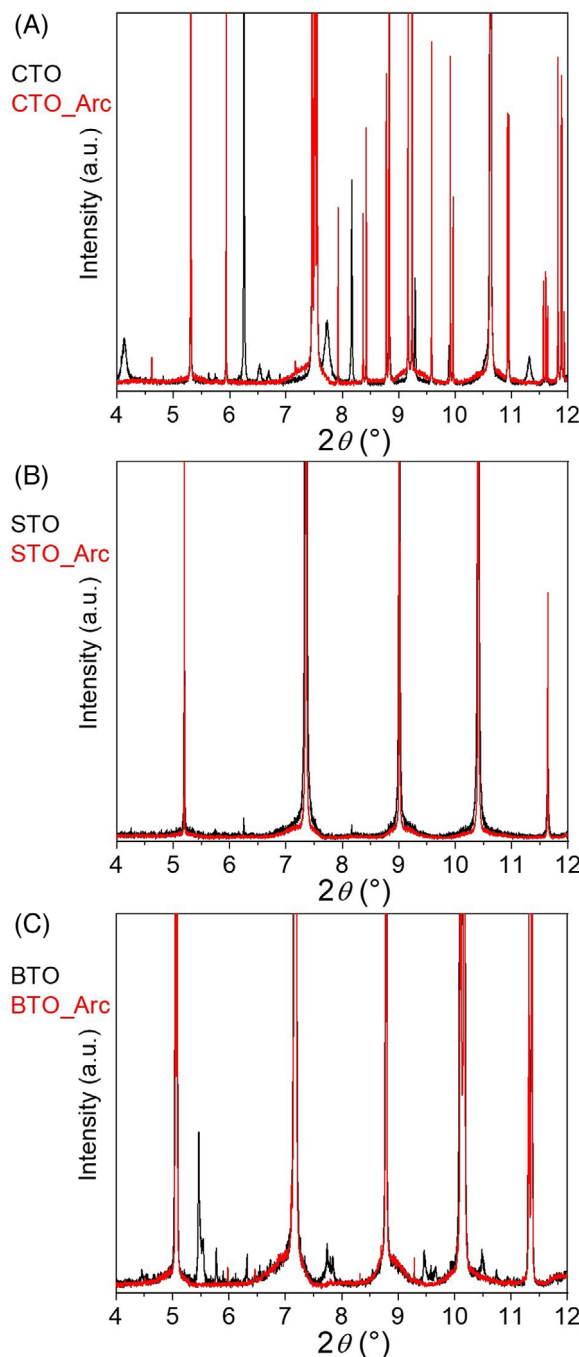


**FIGURE 1** Powder X-ray diffraction pattern ( $\lambda = 0.35439$  Å) of (A) CTO and CTO\_arc, (B) STO and STO\_arc, and (C) BTO and BTO\_arc obtained at room temperature. Intensity is plotted on a logarithmic scale for better visibility of low-intensity peaks. Secondary phases were hardly detectable by laboratory X-ray diffractometers, but these secondary phases were detected by synchrotron radiation.

were identified, that is,  $\text{Ca(OH)}_2$  for CTO and  $\text{BaCO}_3$  for BTO. In order to determine the crystal structural parameters and atomic structural parameters, Rietveld analysis was conducted and the results are presented in Supporting Information S4–S6.

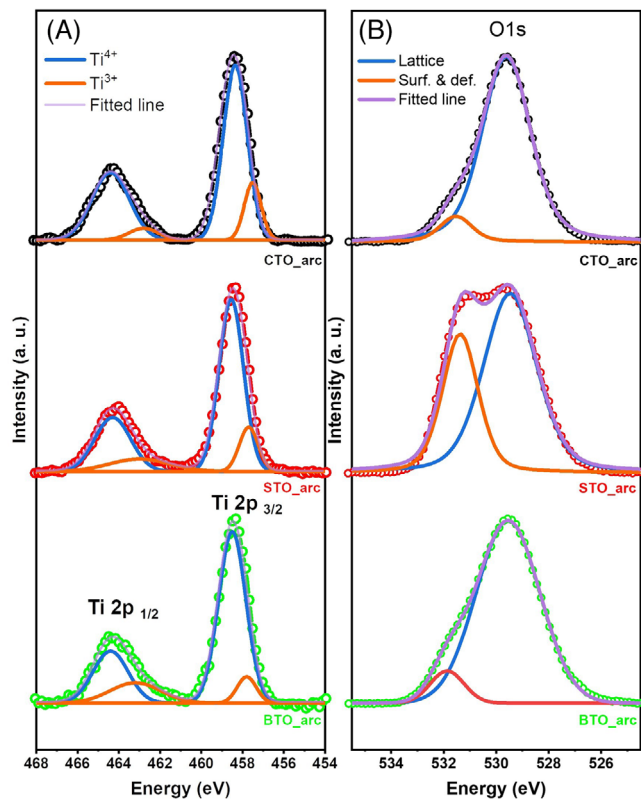


FIGURE 2 X-ray photoemission spectra (background subtracted) at (A) Ti 2*p* and (B) O 1*s* of CTO\_arc (black), STO\_arc (red), and BTO\_arc (green).

For a chemical element analysis, XPS was carried out. The Ti 2*p* and O 1*s* XPS spectra of three arc-melted samples are presented in Figure 2 after the background was subtracted from the spectra. The characteristic Ti 2*p*<sub>3/2</sub> peak can be deconvoluted into two curves for Ti<sup>4+</sup> (blue lines, binding energy of 458.6 eV) and Ti<sup>3+</sup> (orange lines, binding energy of 457.7 eV) as shown in Figure 2A. The ratio of Ti<sup>3+</sup>/Ti<sup>4+</sup> from the XPS spectra is calculated to be 19.5 % for CTO\_arc, 25.7 % for STO\_arc, and 28.7 % for BTO\_arc, respectively. The O 1*s* XPS spectra shown in Figure 2B are fitted by two peaks centered at 529.5 eV and 531.2 eV, which are attributed to the lattice oxygen (marked as Lattice) and surface adsorbed oxygen with oxygen deficiency (marked as Surf. & def.), respectively. The concentrations of oxygen deficiencies in CTO\_arc and BTO\_arc were ca. 10 %, while that of STO\_arc was ca. 40 % which deviates from the generally expected maximum range of deficiency for perovskite. The estimated high deficiency of oxygen could be originated from oxygen-containing species on the surface of STO\_arc such as OH<sup>-</sup>, H<sub>2</sub>O, CO<sub>2</sub>/CO<sub>3</sub><sup>2-</sup> as well as oxygen vacancies. The survey scan and XPS spectra for CTO, STO, and BTO before arc-melting are also provided in Supporting Information S7 and S8.

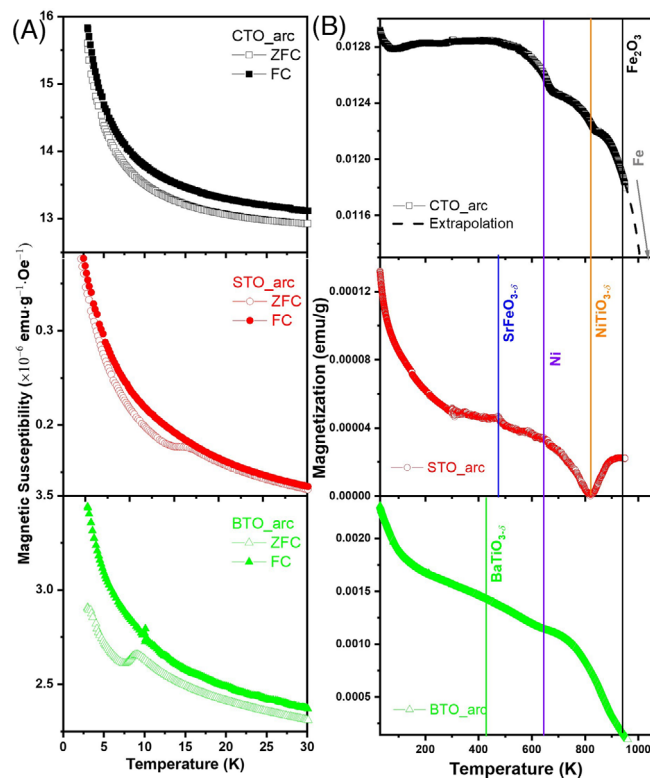


FIGURE 3 Temperature dependence of (A) susceptibility at low temperature and (B) magnetization measured at high temperature under an external field of 0.1 T. CTO\_arc (black), STO\_arc (red), and BTO\_arc (green). The critical temperatures, that is, Curie or Néel temperature, of possible secondary phases are highlighted by vertical lines.

Temperature-dependent susceptibility  $\chi$  (*M-T* curves) at low temperatures are shown in Figure 3A. With decreasing temperature, the susceptibility increased and the values at 3 K are about one order of magnitude higher than those at room temperature. The absolute value decreased in the order CTO\_arc > BTO\_arc > STO\_arc. The susceptibilities exhibited typical ferromagnetic behavior with a bifurcation between FC and ZFC magnetization curves. Bifurcation temperatures were estimated to be ~150 K for CTO\_arc, ~200 K for STO\_arc, and ~180 K for BTO\_arc, respectively. Additionally, ZFC curves of STO\_arc and BTO\_arc exhibited magnetic phase transition with critical blocking temperatures ( $T_B$ ) of 16 and 9 K, respectively. Below  $T_B$ , magnetic nanoparticles exhibit hysteresis due to metastability induced by insufficient time for complete magnetic relaxation when superparamagnetic samples are cooled.<sup>27</sup> Pei et al. also reported the emergent magnetic phase transition near 18 K in the Fe-doped SrTiO<sub>3- $\delta$</sub> .<sup>28</sup>  $T_B$  was not observed for pristine STO and BTO (Supporting Information S9).

Figure 3B displays *M-T* curves at high temperatures. *M-T* curves exhibited several critical temperatures from



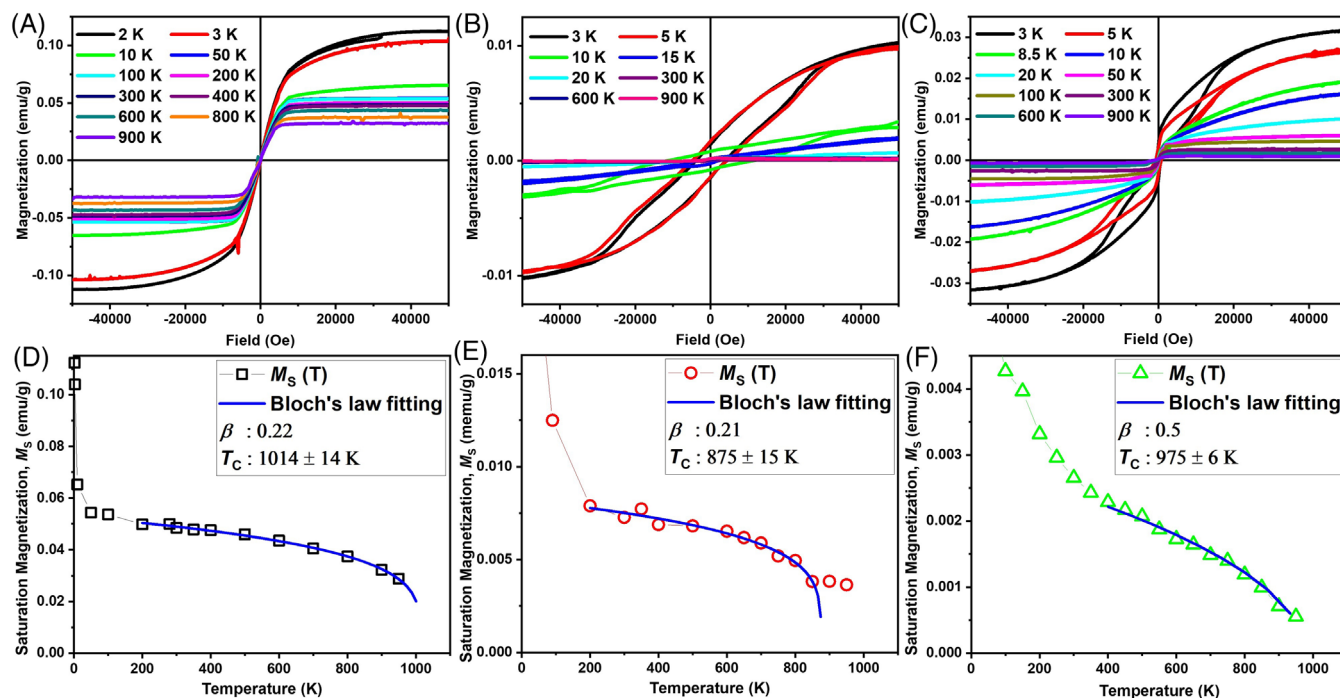
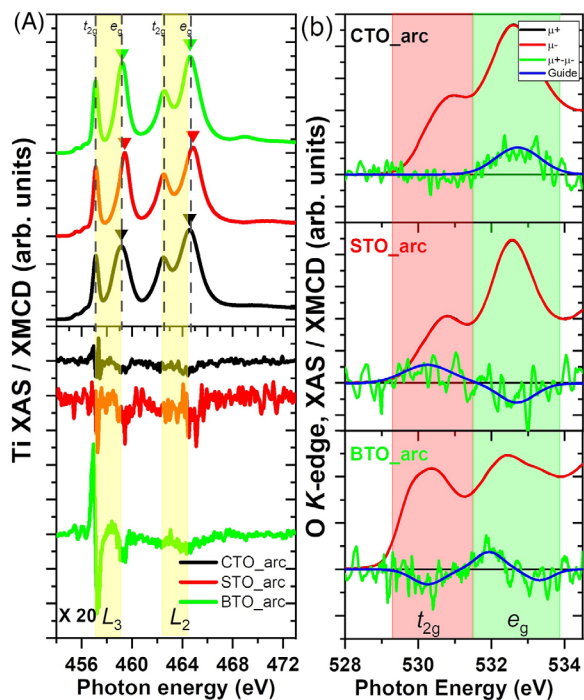


FIGURE 4 Field dependence of magnetization at various temperatures and the fitting results of the saturation magnetization with Bloch's law for (A, D) CTO\_arc, (B, E) STO\_arc, and (C, F) BTO\_arc, respectively.

which the compounds can be inferred. From the extrapolation of the  $M-T$  curve, the Curie temperature is calculated to be  $\sim 1000$  K for CTO\_arc. CTO\_arc also showed steps that might be assigned to  $\text{NiTiO}_3$ ,  $\text{Fe}_2\text{O}_3$ , and  $\text{Ni}$ .<sup>29–31</sup> Thus, it is concluded that the substitution of impurities such as Fe or Ni at the Ti site in the  $\text{CaTiO}_3$  perovskite structure was hardly possible for CTO\_arc. On the other hand, in the case of STO\_arc signatures that might belong to  $\text{SrFeO}_3$  and  $\text{NiTiO}_3$  were observed,<sup>32,33</sup> revealing that the Sr and Ti sites are selectively substituted by Ni and Fe, respectively. Finally, in the case of BTO\_arc apparently, there is no peak due to the substitution of the magnetic transition element. Critical temperatures of Fe and Co metals are reported to be higher than 1000 K, which was out of the measurement range in this study. The differentiation ( $dM/dT$ ) data as a function of temperature over the range of 320–945 K shown in Supporting Information S10 revealed the peaks of phase transition at different critical temperatures, and the critical temperatures of corresponding materials are summarized in Supporting Information S11.

Field-dependent magnetization curves ( $M-H$ ) of CTO\_arc, STO\_arc, and BTO\_arc are presented in Figure 4. The raw data were corrected considering the para- and diamagnetic terms by a linear fitting at high magnetic fields.  $M-H$  curves of CTO, STO, and BTO with paramagnetic correction are shown in Supporting Information S12. In addition, the  $M-H$  curves of arc-melted samples without correction at low temperatures are shown in Supporting Information S13. CTO\_arc showed

the highest magnetization value among all arc-melted and pristine samples. The hysteresis loops were also confirmed for CTO\_arc, STO\_arc, and BTO\_arc. The soft and hard magnetic components were observed to be exchange-coupled with each other for STO\_arc. The soft and hard magnetic materials could be distinguished by coercivity where soft magnetic material has no coercivity, while hard magnet has coercivity. The coupled magnet shows a hysteresis loop without any step. De-coupled magnets, on the other hand, have steps in hysteresis loops. Interestingly, the magnetic decoupling was obviously observed at 3 K for BTO\_arc. This finding of coupling in STO\_arc and decoupling in BTO\_arc in  $M-H$  curves indicates that both soft and hard magnetic compounds formed in STO\_arc and BTO\_arc interplay differently. In the case of STO\_arc, the magnetic exchange interaction occurs inside the perovskite structure, whereas in the case of BTO\_arc, the exchange interaction is outside of the perovskite, namely between the perovskite and secondary phase. The saturation magnetization of  $M-H$  curves at various temperatures was fitted with Bloch's law  $M(T) = A(T - T_C)^\beta$  as shown in Figure 4D–F.<sup>34</sup>  $T_C$  is the ordering temperature, i.e. the Curie temperature in a ferromagnet or the Néel temperature in an antiferromagnet and  $\beta$  is the critical exponent that reflects the universality class and actual dimensionality of the magnetic system. BTO\_arc was fitted well as a three-dimensional bulk ferromagnet ( $\beta$ ) which can be explained by the existence of binary  $TM$ -oxides ( $TM = \text{Fe}, \text{Co}, \text{and Ni}$ ). The fitting



**FIGURE 5** Normalized X-ray absorption spectroscopy (XAS) (top) and X-ray magnetic circular dichroism (XMCD) (bottom) edge spectra for CTO\_arc (black), STO\_arc (red), and BTO\_arc (green) are shown at (A) the Ti  $L_{2,3}$ -edges (The vertical dashed lines are guides for the eyes) and (B) the O  $K$ -edge measured at room temperature.

results of CTO\_arc and STO\_arc, however, revealed two dimensional  $XY$  magnet system with the  $\beta$  value of ca. 0.221 and 0.214, respectively.<sup>35</sup> In CTO\_arc, the Ca site is supposed to be substituted by magnetic elements. In STO\_arc, the magnetic transition metal elements most likely substitute into both the Sr site and Ti site after arc-melting. Finally, in BTO\_arc there is no evidence of the substitution, but the hard magnet is found to be formed as a secondary phase in  $M$ – $H$  curve at low temperature. The value of  $\beta$  was 0.5 indicating 3-D ferromagnet phase. This finding is in good agreement with the  $M$ – $T$  curve analysis exhibited in Figure 3B.

Normalized XAS and XMCD spectra at the Ti  $L_{2,3}$ -edge are shown in Figure 5A. The contribution of  $Ti^{3+}$  is evidenced by the reduced energy difference between  $t_{2g}$  and  $e_g$ , and by the broadened  $e_g$  peak width.<sup>36</sup> CTO\_arc displayed the smallest energy difference between  $t_{2g}$  and  $e_g$  together with the largest  $e_g$  peak broadening among three samples. On the other hand, the XAS spectra of STO\_arc revealed the biggest energy difference between  $t_{2g}$  and  $e_g$ . A more detailed comparison of spectra can be seen in Supporting Information S14. The contribution of  $Ti^{3+}$  to the magnetism of  $ATiO_{3-\delta}$  ( $A = Ca, Sr, Ba$ ) is also revealed in the XMCD spectra. The total magnetic moment of Ti is obtained by the sum rule and the details of the

analysis are presented in Supporting Information S15. The oxidation state of Ti 3d can be indirectly confirmed by the XMCD measurement at the O  $K$ -edge as shown in Figure 5B.<sup>37</sup> There are multifold contributions for the signal at O  $K$ -edges from various compounds including the perovskite itself and binary transition metal oxides. In the case of CTO\_arc,  $e_g$  dominant MCD peak ( $\mu^+ - \mu^-$ , shown in green) is observed, which is highly related to magnetic transition metal oxide, not to the perovskite itself. This is in good agreement with  $M$ – $T$  and  $M$ – $H$  curves analysis shown in Figures 3 and 4, respectively. On the other hand, STO\_arc and BTO\_arc had both  $t_{2g}$  and  $e_g$  MCD peaks with a marginal difference and the peaks are in opposite directions. In the case of STO\_arc, the antiferromagnetic ordering of  $SrFeO_{3-\delta}$  appears to contribute to the spectra where Ti-oxygen-Fe bonding can explain the induced  $t_{2g}$  peak from Ti and  $e_g$  peak by Fe, respectively. In the case of BTO\_arc,  $t_{2g}$  MCD peak dominantly originated from the  $Ti^{3+}$  ferromagnetism and  $e_g$  peak is shown to be the superposition of two peaks whose origin is assumed to be from Ti-oxygen-Ti in the perovskite structure and the contribution outside of the perovskite lattice like  $Fe_2O_3$  expected to be present in BTO\_arc. Due to the highly reducing condition, arc-melted samples have  $Ti^{3+}$  ions which are also highly correlated with oxygen vacancy in the perovskite structure. The XMCD intensities revealed that  $Ti^{3+}$  concentration is directly proportional to the  $\delta$  values of all the arc-melted titanates, and the details are shown in Supporting Information S16.

## 4 | DISCUSSION

For a better understanding of the magnetic properties of arc-melted titanates, the obtained experimental results were carefully correlated. For a consistent picture, the existence of magnetic impurity phases has to be experimentally proven. Notably, magnetic impurity phases play a non-negligible role even when the concentrations are in the range of parts per million (ppm,  $10^{-6}$ ).<sup>21,22,38–40</sup> For the identification of Fe, Co, and Ni, ICP-OES was carried out and summarized in Supporting Information S16. The results indicate that the magnetic properties obtained in this study can be highly influenced by the existing magnetic impurities existed in precursor powders. The crucial observation is that CTO\_arc showed one order of magnitude higher susceptibility value than CTO (Figure 3 and Figure S9). STO and BTO also possess similar amounts of magnetic impurities, but the magnetization value does not change significantly after arc melting. The magnetization behavior of CTO is different from the other two perovskites in this study. The interpretation of this different magnetization behavior is not straightforward. Nevertheless, it

is concluded that depending on the site-selectivity of the magnetic *3d* impurities such as Fe, Co, and Ni magnetism hugely varied in arc-melted perovskite titanates.

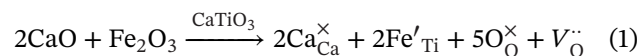
Notably, the secondary phases are only visible in the pristine white powders by synchrotron XRD as shown in Supporting Information S3. The reflections which do not belong to the perovskite phase vanished after arc-melting. Rearrangement and reconstruction of perovskite crystal lattice happened together with the possible incorporation of magnetic impurities. In addition, during the arc melting (fast heating, melting, and quenching under the Ar atmosphere), a severe reduction reaction happened. Thus, the substitution of magnetically active *3d* elements is highly related to the thermodynamic and dynamic stability of the perovskite structure. No detectable magnetic phase was confirmed by synchrotron XRD after arc-melting, i.e. the other binary oxide phases, if any, are too small to be detected even in synchrotron XRD. By XPS and XAS, the ratios of  $Ti^{3+}/Ti^{4+}$  in titanates were verified, and the ratios of  $Ti^{3+}/Ti^{4+}$  increased in the order of CTO\_arc < STO\_arc < BTO\_arc consistent with the order of oxygen vacancy  $\delta$  values in ICP-OES. In order to quantify the *3d* impurities and  $Ti^{3+}$  concentration more accurately, electron paramagnetic resonance experiments can be executed hereafter.<sup>41</sup>

As presented, the generation of oxygen vacancies together with the reduction of  $Ti^{4+}$  is expected during arc-melting. Furthermore, with the substitution of magnetic impurities on the Ti site, complicated evolution of *M-T* and *M-H* curves is expected. When Ti is substituted by Fe in  $SrTiO_{3-\delta}$ , for instance, non-monotonic change with a decreasing temperature in the *M-T* curve and the hysteresis feature in the *M-H* curve had been already reported.<sup>28</sup> The small discrepancies between experimental observations in this study and the previous report both the blocking temperatures in the *M-T* curve and the coercive field value in the *M-H* curve can be explained by the different types and amounts of magnetic impurities. Maikhuri et al. reported different ferromagnetic behavior in case of *A*- and *B*-site Fe substituted  $BaTiO_3$ .<sup>42</sup> Our *M-T* curve showed a similar hysteresis loop to that of *B*-site substitution in  $BaTiO_3$ . However, our *M-H* curve of BTO\_arc revealed decisive magnetic decoupling that can be explained by the existence of separated two phases like  $BaTiO_3$  and  $Fe_2O_3$ .

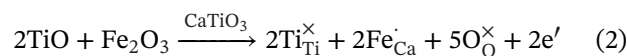
In contrast to STO and BTO, our results show that *A*-site substitution is much more plausible for CTO, suggesting that not only the concentration of oxygen vacancies and  $Ti^{3+}$ ,<sup>43</sup> but also the site occupation of magnetic ions in these perovskite titanates  $ATiO_{3-\delta}$  (*A* = Ca, Sr, Ba) impact the resulting magnetic properties.

The ionic radius of octahedral  $Fe^{3+}$  is close to that of  $Ti^{4+}$ , thus *B*-site substitution is expected ( $r(Fe^{3+})_{VI, high spin} = 0.645 \text{ \AA}$ , and  $r(Ti^{4+})_{VI} = 0.605$

$\text{\AA}$ ). However, the ionic radius of  $Fe^{2+}$  is in between the ionic radius values of  $Ca^{2+}$  and  $Ti^{4+}$  ( $r(Ca^{2+})_{XII} = 1.34 \text{ \AA}$ ,  $r(Fe^{2+})_{VI, high spin} = 0.78 \text{ \AA}$ , and  $r(Ti^{4+})_{VI} = 0.605 \text{ \AA}$ ).<sup>44</sup> In the viewpoint of defect chemistry, Fe substitution for Ti site in  $CaTiO_3$  can be described as (Eq. 1) with Kröger-Vink notation,<sup>45</sup>



This implies that the Fe substitution would generate more oxygen vacancies. On the contrary, Fe substitution for the Ca site in  $CaTiO_3$  can be described as (Eq. 2)



The observed ferromagnetic behavior in  $CaTiO_3$  can be connected with  $V''_{Ca}$ .<sup>46</sup> It is postulated that Ca vacancies first formed during arc-melting and subsequently unstable  $Ca_{1-x}TiO_3$  favored the facilitation of Fe on Ca-site.

Contrary to CTO, STO preferred the *B*-site substitution and BTO showed substitution of magnetic impurities is hardly detectable with increased concentration of oxygen vacancies (hot gas extraction result) and  $Ti^{3+}$  (XMCD result). This difference originated from the structural stability and formability of perovskite titanates. The stability and distortion of the perovskite-type crystal structures can be typically described by Goldschmidt's tolerance factor *t*

$$t = \frac{r_A + r_O}{\sqrt{2}(r_{Ti} + r_O)} \quad (3)$$

where *r* is the ionic radius of ion and the ideal cubic structure can be observed when *t* is close to 1.<sup>47,48</sup> Goldschmidt's tolerance factor *t* of  $CaTiO_3$ ,  $SrTiO_3$ , and  $BaTiO_3$  are 0.966, 1.001, and 1.062, respectively based on the effective ionic radii of Shannon & Prewitt.<sup>44</sup> CTO\_arc, STO\_arc, and BTO\_arc were indexed to orthorhombic, cubic, and tetragonal structures, respectively. Typically, charge compensation is achieved by the reduction of  $Ti^{4+}$  to  $Ti^{3+}$  ions when oxygen vacancies are formed. In other words, due to the oxygen vacancies commonly generated in  $SrTiO_3$ , adjacent Ti ions are reduced from  $Ti^{4+}$  to  $Ti^{3+}$ , which form an orbital state below the bottom of the conduction band. The magnetization is proclaimed to appear because of this spin-split impurity bands in the insulating  $SrTiO_3$  matrix. In this study, the ferromagnetism of titanates can be partly attributed to the creation of surface or lattice oxygen vacancies. The effective magnetic moment per  $Ti^{3+}$  ions has been verified by XMCD, confirming that adjacent Ti ions are reduced from  $Ti^{4+}$  to  $Ti^{3+}$ .

From the observations above, it was concluded that the dominant contribution to the ferromagnetic behavior is made not by the local magnetic moments of the  $Ti^{3+}$  ( $3d^1$ ) ions or associated oxygen vacancies, but by the magnetic



3d impurities whose site occupation is governed by crystal structural aspects in the perovskite lattice. Differentiation of the contribution of extrinsic magnetic ions, intrinsic  $Ti^{3+}$ , and oxygen vacancies is intriguing, and an open question remains to be investigated. Further studies would be necessary to address this issue in more detail. For example, in order to control the oxygen vacancies and concentration of  $Ti^{3+}$  without affecting the contribution of extrinsic magnetic ions an annealing experiment in a quartz tube would be anticipated. With this, magnetic properties can be investigated and correlated with the effect of oxygen vacancies and concentration of  $Ti^{3+}$ .

## 5 | SUMMARY

Arc-melted perovskites were successfully synthesized without any detectable secondary phases even with synchrotron XRD. Crystal structure and magnetic properties were investigated. CTO<sub>arc</sub> showed one order of magnitude higher susceptibility than pristine CTO. The origin of the magnetism in perovskite titanates  $ATiO_{3-\delta}$  ( $A = Ca, Sr, Ba$ ) was interpreted with respect to the occupational preference of magnetic impurities in the perovskite structure during arc melting. Both, the formation of oxygen vacancies and reduction of  $Ti^{4+}$  to  $Ti^{3+}$  play minor roles in magnetic properties as proven by XPS and XMCD. The structural stability and formability of perovskite titanates are found to influence the predetermined occupation of magnetic impurities and reduction behavior in these particular three perovskite compounds  $ATiO_{3-\delta}$  ( $A = Ca, Sr, Ba$ ).

## ACKNOWLEDGMENTS

The authors are grateful to European Synchrotron Radiation Facility (ESRF), the synchrotron light source KARA and the Karlsruhe Nano Micro Facility (KNMF) for the provision of beamtimes. The authors are indebted to Mr. Samir Hammoud at the Max Planck Institute for Intelligent Systems for the chemical analysis (ICP-OES, hot gas extraction). Open Access funding enabled and organized by Project DEAL.

Open access funding enabled and organized by Projekt DEAL.

## ORCID

Wenjie Xie  <https://orcid.org/0000-0003-1826-7574>

Kwanghyo Son  <https://orcid.org/0000-0002-4751-2885>

## REFERENCES

- Mitchell RH. Perovskites: modern and ancient. Thunder Bay, Ont: Almaz Press; 2002.
- Suntivich J, Gasteiger HA, Yabuuchi N, Nakanishi H, Goodenough JB, Shao-Horn Y. Design principles for oxygen-reduction activity on perovskite oxide catalysts for

- fuel cells and metal-air batteries. *Nat Chem*. 2011;3:546–50. <https://doi.org/10.1038/nchem.1069>
- Kageyama H, Hayashi K, Maeda K, Attfield JP, Hiroi Z, Rondinelli JM, et al. Expanding frontiers in materials chemistry and physics with multiple anions. *Nat Commun*. 2018;9:772. <https://doi.org/10.1038/s41467-018-02838-4>
- Nishihata Y, Mizuki J, Akao T, Tanaka H, Uenishi M, Kimura M, et al. Self-regeneration of a Pd-perovskite catalyst for automotive emissions control. *Nature*. 2002;418:164–7. <https://doi.org/10.1038/nature00893>
- Neagu D, Tsekouras G, Miller DN, Ménard H, Irvine JTS. In situ growth of nanoparticles through control of non-stoichiometry. *Nat Chem*. 2013;5:916–23. <https://doi.org/10.1038/nchem.1773>
- Brown JJ, Ke Z, Geng W, Page AJ. oxygen vacancy defect migration in titanate perovskite surfaces: effect of the A-site cations. *J Phys Chem C*. 2018;122:14590–7. <https://doi.org/10.1021/acs.jpcc.8b03322>
- Dawson JA. Dynamical insights into oxygen diffusion in BaTiO3 and SrTiO3. *Phys Status Solidi B*. 2020;257:1900422. <https://doi.org/10.1002/pspb.201900422>
- Eichel R-A. Structural and dynamic properties of oxygen vacancies in perovskite oxides—analysis of defect chemistry by modern multi-frequency and pulsed EPR techniques. *Phys Chem Chem Phys*. 2011;13:368–84. <https://doi.org/10.1039/B918782K>
- Li C-Q, Yi S-S, Chen D, Liu Y, Li Y-J, Lu S-Y, et al. Oxygen vacancy engineered SrTiO3 nanofibers for enhanced photocatalytic H2 production. *J Mater Chem A*. 2019;7:17974–80. <https://doi.org/10.1039/C9TA03701B>
- Zu D, Wang H, Lin S, Ou G, Wei H, Sun S, et al. Oxygen-deficient metal oxides: synthesis routes and applications in energy and environment. *Nano Res*. 2019;12:2150–63. <https://doi.org/10.1007/s12274-019-2377-9>
- Kovačić M, Stopar K, Vertnik R, Šarler B. Comprehensive electric arc furnace electric energy consumption modeling: a pilot study. *Energies*. 2019;12:2142. <https://doi.org/10.3390/en12112142>
- Populoh S, Brunko OC, Gałazka K, Xie W, Weidenkaff A. Half-Heusler (TiZrHf)NiSn unileg module with high powder density. *Materials*. 2013;6:1326–32. <https://doi.org/10.3390/ma6041326>
- Ou G, Li D, Pan W, Zhang Q, Xu B, Gu L, et al. Arc-melting to narrow the bandgap of oxide semiconductors. *Adv Mater*. 2015;27:2589–94. <https://doi.org/10.1002/adma.201405763>
- Chen X, Liu L, Huang F. Black titanium dioxide (TiO2) nanomaterials. *Chem Soc Rev*. 2015;44:1861–85. <https://doi.org/10.1039/C4CS00330F>
- Lin T, Yang C, Wang Z, Yin H, Lü X, Huang F, et al. Effective nonmetal incorporation in black titania with enhanced solar energy utilization. *Energy Environ Sci*. 2014;7:967–72. <https://doi.org/10.1039/C3EE42708K>
- Sunstrom JE, Kauzlarich SM, Klavins P. Synthesis, structure, and properties of lanthanum strontium titanate (La1-xSrxTiO3) (0 ≤ x ≤ 1). *Chem Mater*. 1992;4:346–53. <https://doi.org/10.1021/cm00020a022>
- Ju HL, Eylem C, Peng JL, Eichhorn BW, Greene RL. Metal-insulator transitions and weak ferromagnetism in the electron-correlated system Nd1-xCaxTiO3 (0 ≤ x ≤ 1). *Phys Rev B*. 1994;49:13335. <https://doi.org/10.1103/PhysRevB.49.13335>
- Connolly EJ, Tilley R. Electrical properties of the arc-melted, layered-perovskite system NdnTinO3n+2 with n = 4.5–6.5. *J*



- Alloys Compd. 2012;515:63–7. <https://doi.org/10.1016/j.jallcom.2011.11.044>
19. Gu L, Wei H, Peng Z, Wu H. Defects enhanced photocatalytic performances in SrTiO<sub>3</sub> using laser-melting treatment. *J Mater Res.* 2017;32:748–56. <https://doi.org/10.1557/jmr.2016.461>
  20. Yu W, Ou G, Si W, Qi L, Wu H. Defective SrTiO<sub>3</sub> synthesized by arc-melting. *Chem Comm.* 2015;51:15685–8. <https://doi.org/10.1039/C5CC06371J>
  21. Coey JMD, Venkatesan M, Fitzgerald CB. Donor impurity band exchange in dilute ferromagnetic oxides. *Nat Mater.* 2005;4:173–9 <https://doi.org/10.1038/nmat1310>
  22. Coey JMD. Magnetism in d0 oxides. *Nat Mater.* 2019, 18:652–6. <https://doi.org/10.1038/s41563-019-0365-9>
  23. Zhang Y, Hu J, Cao E, Sun L, Qin H. Vacancy induced magnetism in SrTiO<sub>3</sub>. *J Magn Magn Mater.* 2012;324:1770–5. <https://doi.org/10.1016/j.jmmm.2011.12.036>
  24. Potzger K, Osten J, Levin AA, Shalimov A, Talut G, Reuther H, et al. Defect-induced ferromagnetism in crystalline SrTiO<sub>3</sub>. *J Magn Magn Mater.* 2011;323:1551–62. <https://doi.org/10.1016/j.jmmm.2011.01.018>
  25. Rao SS, Lee YF, Prater JT, Smirnov AI, Narayan J., Laser annealing induced ferromagnetism in SrTiO<sub>3</sub> single crystal. *Appl Phys Lett.* 2014;105:042403. <https://doi.org/10.1063/1.4891184>
  26. Dejoie C, Coduri M, Petitdemange S, Giacobbe C, Covacci E, Grimaldi O, et al. Combining a nine-crystal multi-analyser stage with a two-dimensional detector for high-resolution powder X-ray diffraction. *J Appl Crystallogr.* 2018;51:1721–33. <https://doi.org/10.1107/S1600576718014589>
  27. Majetich SA, Wen T, Mefford OT. Magnetic nanoparticles. *MRS Bull.* 2013;38:899–903 <https://doi.org/10.1557/mrs.2013.230>
  28. Pei Y, Zhang R, Song Y, Bi J, Xu W, Zhou C, et al. Emergent magnetic phase transitions in Fe-doped SrTiO<sub>3</sub>– $\delta$ . *AIP Adv.* 2019;9:125302. <https://doi.org/10.1063/1.5116671>
  29. Mona J, Kale SN, Gaikwad AB, Murugan A, Ravi V., Chemical methods to synthesize FeTiO<sub>3</sub> powders. *Mater Lett.* 2006;60:1425–7. <https://doi.org/10.1016/j.matlet.2005.11.041>
  30. Yamaki K, Shimizu N, Kita E, Mochiku T, Fujii H, Yamada K, et al. Ferromagnetism in Co-doped TiO<sub>2</sub> single crystals. *Phys Status Solidi C.* 2007;3(12):4127–30. <https://doi.org/10.1002/pssc.200672876>
  31. Bahadur N, Pasricha R, Govind CS, Mater KRK. Effect of Ni doping on the microstructure and high Curie temperature ferromagnetism in sol-gel derived titania powders. *Chem Phys.* 2012;133:471–9. <https://doi.org/10.1016/j.matchemphys.2012.01.068>
  32. Tsujimoto Y, Tassel C, Hayashi N, Watanabe T, Kageyama H, Yoshimura K, et al. Infinite-layer iron oxide with a square-planar coordination. *Nature* 2007;450:1062–5. <https://doi.org/10.1038/nature06382>
  33. Takeda T, Watanabe H. Magnetic Properties of the System SrCo<sub>1-x</sub>FexO<sub>3-y</sub>. *J Phys Soc Japan.* 1972;33:973–8. <https://doi.org/10.1143/JPSJ.33.973>
  34. Kraftmakher Y. Curie point of ferromagnets. *Eur. J Phys.* 1997;18:448. <https://doi.org/10.1088/0143-0807/18/6/008>
  35. Bramwell ST, Holdsworth PCW. Magnetization and universal sub-critical behaviour in two-dimensional XY magnets. *J Phys Condens Matter.* 1993;5:L53–9. <https://doi.org/10.1088/0953-8984/5/4/004>
  36. Garcia-Barriocanal J, Cezar JC, Bruno FY, Thakur P, Brookes NB, Utfeld C, et al. Spin and orbital Ti magnetism at LaMnO<sub>3</sub>/SrTiO<sub>3</sub> interfaces. *Nat Commun.* 2010;1:82. <https://doi.org/10.1038/ncomms1080>
  37. Lee J-S, Xie YW, Sato KH, Bell C, Hikita Y, Hwang HY, et al. Titanium dxy ferromagnetism at the LaAlO<sub>3</sub>/SrTiO<sub>3</sub> interface. *Nat Mater.* 2013;12:703–6. <https://doi.org/10.1038/nmat3674>
  38. Coey JMD, Venkatesan M, Stamenov P. Surface magnetism of strontium titanate. *J Phys Condens Matter.* 2016;28:485001. <https://doi.org/10.1088/0953-8984/28/48/485001>
  39. Coey JMD. d0 ferromagnetism. *Solid State Sci.* 2005;7:660–7. <https://doi.org/10.1016/j.solidstatesciences.2004.11.012>
  40. Coey JMD, Stamenov P, Gunning RD, Venkatesan M, Paul K. Ferromagnetism in defect-ridden oxides and related materials. *New J Phys.* 2010;12:53025. <https://doi.org/10.1088/1367-2630/12/5/053025>
  41. Zhang J, Ji L, Jia X, Wang J, Zhai J, Zhou Y. Crystal structure and effective dielectric response of Ba<sub>0.5</sub>Sr<sub>0.5</sub>TiO<sub>3</sub>–MgO composites synthesized in situ process. *J Am Ceram Soc.* 2015;98:97–103. <https://doi.org/10.1111/jace.13242>
  42. Maikhuri N, Panwar AK, Jha AK. Investigation of A- and B-site Fe substituted BaTiO<sub>3</sub> ceramics. *J Appl Phys.* 2013;113:17D915. <https://doi.org/10.1063/1.4796193>
  43. Yoon S, Son K, Ebbinghaus SG, Widenmeyer M, Weidenkaff A. Ferromagnetism in nitrogen and fluorine substituted BaTiO<sub>3</sub>. *J Alloys Compd.* 2018;749:628–33. <https://doi.org/10.1016/j.jallcom.2018.03.221>
  44. Shannon RD. Revised effective ionic radii and systematic studies of interatomic distances in halides and chalcogenides. *Acta Cryst.* 1976;A32:751–67. <https://doi.org/10.1107/S0567739476001551>
  45. Kröger FA, Vink HJ. In: Seitz F, Turnbull D, editors. *Solid state physics: advances in research and applications. Relations between the Concentrations of Imperfections in Crystalline Solids*, New York: Academic Press; 1956. p. 307.
  46. Sun L, Zhang Y, Ju L, Shi C, Qin H, Hu J. Cation vacancy-induced ferromagnetism in nanocrystalline CaTiO<sub>3</sub> plate. *IEEE Trans Magn.* 2014;50:2303404 <https://doi.org/10.1109/TMAG.2014.2329714>
  47. Goldschmidt VM. *Die Gesetze der Krystallochemie*. *Naturwissenschaften.* 1926;14:477–85 <https://doi.org/10.1007/BF01507527>
  48. Bartel CJ, Sutton C, Goldsmith BR, Ouyang R, Musgrave CB, Ghiringhelli LM, et al. New tolerance factor to predict the stability of perovskite oxides and halides. *Sci Adv.* 2019;5:eaav0693. <https://doi.org/10.1126/sciadv.aav0693>

## SUPPORTING INFORMATION

Additional supporting information can be found online in the Supporting Information section at the end of this article.

**How to cite this article:** Yoon S, Xie W, Xiao X, Checchia S, Coduri M, Schuetzenduebe P, et al. Site-selective substitution and resulting magnetism in arc-melted perovskite ATiO<sub>3- $\delta$</sub>  (A = Ca, Sr, Ba). *J Am Ceram Soc.* 2023;106:6778–6786. <https://doi.org/10.1111/jace.19308>